Thermal properties of Ag@Ni core-shell nanoparticles

Vit Vykoukal [a,b,*], Frantisek Zelenka [a], Jiri Bursik [c], Tomas Kana [c,d], Ales Kroupa [c], Jiri Pinkas [a,b]

[a] Masaryk University, Faculty of Science, Department of Chemistry, Kotlarska 2, 611 37, Brno, Czech Republic
[b] Masaryk University, CEITEC MU, Kamenice 5, 625 00, Brno, Czech Republic
[c] Institute of Physics of Materials, ASCR, Zizkova 22, 616 62, Brno, Czech Republic
[d] CEITEC IPM, Institute of Physics of Materials, ASCR, Zizkova 22, 616 62, Brno, Czech Republic

ARTICLE INFO

ABSTRACT

We synthesized Ag@Ni core-shell nanoparticles by the solvothermal hot injection method and characterized them as for their shape and size by dynamic light scattering (DLS), small-angle X-ray scattering (SAXS), and transmission electron microscopy (TEM). We previously demonstrated their core-shell structure by scanning transmission electron microscopy with energy dispersive spectroscopy (STEM-EDS). The silver/nickel phase diagram was calculated by the *CALPHAD* method, and the melting points of 10, 15, and 20 nm silver nano-particles were predicted at 930.2, 940.7, and 946.0 °C, respectively. We took advantage of the nickel shell to avoid silver sintering and to confirm the calculated melting point depression (MPD). The results obtained from the differential scanning calorimetry (DSC) experiments revealed the melting points of 11–15 nm nanoparticles at 944–949 °C in agreement with calculated values.

1. Introduction

Nanoparticles (NPs) of metals and alloys have been intensively studied due to their unique properties, such as a surface plasmon resonance (SPR) [1], magnetic properties [2–4], spinodal decomposition [5], unusual morphologies [6], high catalytic activity [2], and melting point depression (MPD) [7,8]. Together with the predominant experimental approach, the theoretical studies of nanoparticle properties and behavior exist. Both the quantum mechanical approach and the extension of the semiempirical *CALPHAD* method [9–13] are now exploited, but the possibilities of theoretical prediction of properties of nano-materials are limited. The quantum mechanical approaches currently do not allow working with the clusters corresponding to the sizes of experimentally prepared nanoparticles yet, and the *CALPHAD* method is significantly limited by the need for reliable experimental data. Changes in phase transformation temperatures as a function of particle size could be modeled by the *CALPHAD* method [12–14], and these predictions can be verified by thermoanalytical measurements. Such studies has been done for several simple nanosystems, for instance AgSn [15,16], AgSnCu [17,18], CuNi [19], AgCu [20,21], BiSn [22,23], InSn [22], PbSn [22], and BiPb [24] nanoalloys.

Syntheses of nanoalloys and their thermal properties have been intensively studied primarily for the MPD phenomenon which is more noticeable for nanoalloys than for elemental metal nanoparticles [22].

Melting point depression of silver has not been measured for nano-particulate powders, because of low-temperature sintering of silver nanoparticles [25–28]. However, it has been determined for a single nanoparticle by the field emission technique [29] or *in situ* HRTEM [30]. Moreover, MPD could be observed in silver NPs protected by a silica shell [31]. Sintering could also be avoided by encapsulation of nano-particles with metal shells [32] or by embedding them in glass or oxide matrices [33–35]. Nickel is an ideal metal shell because it has a high melting point, is immiscible with silver, and Ag@Ni core-shell nano-particles could be prepared by one-step solvothermal hot injection synthesis [36] in oleylamine. Oleylamine acts as a solvent, reduction, and surface-protective agent at the same time. It also interacts with precursors and in-situ forms more easily decomposable complexes. Despite predicted thermodynamic stability of Ni-core/Ag-shell arrangement [37,38], both Ag@Ni and Ni@Ag types of nanoparticles have been prepared.

In this work, we used a powerful solvothermal hot injection synthesis in oleylamine for the one-step formation of Ag@Ni core-shell structures that were employed for experimental evaluation of the silver melting point depression. We compared the DSC results with the theoretical value predicted by the *CALPHAD* method.

---

2. Experimental

2.1. Materials

Ni(acac)$_2$ (95%) was purchased from Sigma-Aldrich and used as received. AgNO$_3$ was of in-house stock (99.9%). Oleylamine (with the content of 80–90%) and 1-octadecene (90%) were purchased from Sigma-Aldrich, dried over sodium, distilled under reduced pressure and stored in a Schlenk flask with molecular sieves.

2.2. Synthesis of Ag@Ni NPs

The procedure used for the Ag@Ni core-shell NPs preparation was described in detail in our previous work [36]. Briefly, AgNO$_3$ and Ni (acac)$_2$ (in various ratios, the total amount of 0.4 mmol) were dissolved in 4 cm^3 of oleylamine at 85 °C and rapidly injected to a hot mixture (230 °C) of oleylamine and octadecene (a 1 : 1 vol ratio). The reaction was carried out for 10 min; then the reaction mixture was cooled down to laboratory temperature. The Ag@Ni NPs were separated by triple centrifugation and washing with a mixture of hexane and acetone (a 1 : 3 vol ratio) and finally redispersed in hexane.

2.3. Characterization of Ag@Ni NPs

The hydrodynamic diameter (metal core surrounded by an organic shell of surfactant) and size distribution in the form of the polydispersive index (PdI) were determined by the dynamic light scattering (DLS) technique on a Zetasizer Nano ZS (Malvern) instrument in a hexane solution at 25 °C. The samples were diluted and filtered by a syringe filter (pore size 450 nm) to remove aggregates and impurities. Each DLS result is an average of three measurements.

Small-angle X-ray scattering (SAXS) measurements were carried out on a Biosaxs 1000 (Rigaku) system at 25 °C with $\lambda = 14$ nm for 5 min. The samples were sealed in 1.5 mm (O.D.) borosilicate glass capillaries (WJM–Glas). Data were analyzed by both Primus [39] and Gnom [40] software, and the results were mutually compared.

The Ag@Ni NPs were characterized by transmission and scanning electron microscopy (TEM, SEM). The TEM measurements were carried out on a CM12 TEM/STEM (Philips) microscope with EDAX Phoenix EDS and on a JEOL JEM2100F microscope equipped with an energy dispersive spectroscopy (EDS) detector and 10Mpix CCD camera. The samples for the TEM measurements were dispersed in hexane and one drop of the colloidal solution was placed on a holey carbon-coated copper grid and allowed to dry by evaporation at ambient temperature.

For the SEM analysis, the samples were dried at ambient temperature under an inert atmosphere. Analyses were performed on a LYRA 3 XMU FEG/SEM × FIB microscope (Tescan) with an Oxford Instruments X-Max80 analyzer for EDS analyses.

Differential scanning calorimetry (DSC) measurements were carried out on a Netzsch STA 409 CD/3/403/5/G under flowing (70 cm^3 min^{-1}) pure (6N) argon with the heating rate of 10 K min^{-1} from laboratory temperature to 1100 °C. The samples (approx. 20 mg) were placed in Y$_2$O$_3$-coated alumina crucibles covered with a lid. Temperature calibration was carried out with Ag. Uncertainty in the DSC temperature was max. 0.5 °C in repeated runs.

The metal content was analyzed by inductively coupled plasma optical emission spectroscopy (ICP-OES) on an iCAP 6500 Duo (Thermo) spectrometer. The dried AgNi NPs were completely dissolved in HNO$_3$, diluted, and characterized.

3. Theoretical modelling

3.1. Basic principles of the CALPHAD method

It is well known that the particle size in the nanoscale dimension significantly influences the thermodynamics of the systems as the contribution to the total Gibbs energy (GE) from the surface properties of the particle becomes more and more significant. The measurable influence of the surface energy contribution to the GE, e.g., on the melting point depression or the decrease of the temperatures of invariant reactions in the system, exists for the diameter of the particles below 200 nm and the decrease is very significant with decreasing particle size. This behavior can be predicted using the extension of the well-known CALPHAD method [41] towards the modeling of the influence of the nanoparticle dimension on the temperatures of phase transitions (especially the MPD of pure elements and the decrease of the invariant reaction temperatures in more complex systems) [12,13].

The semiempirical CALPHAD method was used for the theoretical modeling of the studied Ag–Ni nanosystem. The models allowing to extend the CALPHAD method also for the describing the particle size influence on the phase diagrams and phase transitions were developed recently [12–14,42,43], and the surface energy contribution to the overall GE of the system was described, mainly for simple binary systems without intermetallic phases. The knowledge of the surface energy contributions is necessary for these calculations, and the existence of experimentally measured surface tension is essential for the calculation of its contribution. Such data generally exist for the liquid elements and alloys, and therefore, the lack of more experimental data limits the exploitation of CALPHAD and the development of general databases.

3.2. Gibbs energy modeling

The modeling of phase diagrams in the CALPHAD method is based on the minimization of total Gibbs energy for a given set of independent variables (e.g., pressure, temperature, overall concentration). The total Gibbs energy is expressed as the weighted sum of Gibbs energies of the individual phases and is summarized in Eq. (1). The individual molar Gibbs energy of any phase G_m^φ is expressed by the additive principle as a sum of particular contributions:

$$G_m^\varphi = G_{ref}^\varphi + G_{id}^\varphi + G_E^\varphi + G_{mag}^\varphi + G_P^\varphi + G_{surf}^\varphi \ldots \tag{1}$$

The first term in the equation is G_{ref}^φ (reference Gibbs energy), the weighted sum of the molar Gibbs energies of all elements or compounds (called the constituents) in the crystallographic structure corresponding to the structure of the modeled phase, relative to the selected reference state (so-called Stable Element Reference – SER state, the value of the actual thermodynamic property of the element in the stable structure at 25 °C and normal pressure, is usually used in the CALPHAD method). The second term $G_{id}^\varnothing$ describes the contribution of ideal mixing to the total Gibbs energy. The deviation of the system from the ideal behavior is described in the third term $G_E^\varnothing$. The next two terms describe the possible contribution from the magnetism or external pressure, if applicable. A detailed description of the Gibbs energy expression can be found, e.g., in Ref. [41].

3.3. The evaluation of the surface energy contribution to the total Gibbs energy

The equation for the expression of the G_{surf}^φ describing the contribution of the surface energy to the total GE was introduced by Refs. [42, 43], and [13]. The former authors used the approach based on the particle curvature, while Kaptay [13] in his comprehensive paper used the number of atoms as an additional variable and came with the expression in the form

$$G_{surf}^\phi = 3 \cdot C \cdot \tau \cdot \frac{V_m}{r} \tag{2}$$

where τ is the surface stress, V_m is molar volume, r is the radius of the (spherical) particle, and C is the shape constant [12]. The coefficient 3 in Eq. (2) substitutes coefficient 2 in the original equation published by Ref. [42] and is based on the work of [13].

The radius r is an independent parameter in Eq. (2), and the molar volume is defined by the crystallographic structure of the studied phase. The surface stress (tension) τ is the crucial quantity for the calculation of the contribution of the surface to the overall GE. This quantity can be measured, and usually reliable data are available for liquid phases of pure elements as well as for some liquid alloys. The calculations of surface stresses for solids and solid solutions can be done using, e.g., the Butler equation, and the software for such calculation was developed by some of the authors in Ref. [44].

Rapid advances of ab-initio methods led to the development of techniques allowing calculation of surface stresses at the level of fundamental quantum mechanics. The advantage of such an approach is the possibility to calculate their values for any element or compound and also for metastable structures. This capability is essential for the *CAL-PHAD* method, as the Gibbs energies of hypothetical compounds or elements in metastable states are necessary for this approach [9,45]. The method for the calculation of surface stress by the ab-initio approach was developed by authors, and it is described in detail in the paper [14]. This method allows calculating the surface stresses not only of solid solutions but also of intermetallic phases, which are generally not available from experimental measurements. Using the ab-initio results, we can calculate the influence of the particle size on the depression of melting and invariant temperatures for more complex systems than are those studied in Ref. [15–24].

4. Results and discussion

4.1. Experimental results

In our previous work [36] we have described in detail the synthesis and morphology of Ag@Ni core-shell nanoparticles. Here we took advantage of the nickel shell to avoid silver sintering and verify the calculated melting point depression. We focused on the characterization of the distribution of sizes, shape, composition, and melting temperatures. Particle diameters were characterized by dynamic light scattering (DLS), based on the intensity of scattered light, and by small-angle X-ray scattering (SAXS). The results are compared in Table 1. The DLS analysis showed hydrodynamic diameters, which represent metal particle cores with an organic shell in a range of 23–32 nm and insignificant dependency of size on chemical composition. Polydispersive index (PdI) in a range of 0.033–0.284 suggests that nanoparticles are relatively monodisperse. The samples analyzed by the SAXS method displayed diameters in a range of 17.6–25.5 nm. These diameters are smaller than in the case of DLS, because SAXS is less sensitive to the organic shell and X-ray is primarily scattered by metal cores. The samples with a silver content of 49 and 59 mol% were too polydisperse for the SAXS analysis. The actual elemental composition was determined by inductively coupled plasma optical emission spectroscopy (Table 1).

Distribution of sizes and shapes were analyzed by transmission electron microscopy (TEM) and results are summarized and displayed in Fig. 1 and Table 1. The TEM analysis of nanoparticles prepared in

various Ag: Ni ratios showed weighted averages in the range of 10.9–15.5 nm. Nanoparticles had regular circular shapes. All results were consistent with our previous work [36] and the dependency of the nanoparticle size on their composition was not observed.

Thermal properties of Ag@Ni nanoparticles were characterized by the differential scanning calorimetry (DSC) method under the inert Ar atmosphere in three heating-cooling cycles (Figs. S1–5). The organic layer at the nanoparticle surface, which acts as a protective shell against aggregation in solution, is thermally decomposed during the first heating cycle. The maximum temperature attained during analysis was 1100 °C, which is higher than the silver melting point but lower than the nickel melting point. The combined effect of the Ag@Ni core-shell morphology and element immiscibility should be that during heating the silver is protected against sintering and above the silver melting point temperature, the nickel shell remains solid protecting the liquid silver core against coagulation. If the nickel shell were continuous and rigid, we should be able to measure melting point depression during all three cycles. The results of the DSC analysis for different elemental compositions are summarized in Table 2.

The DSC-analyzed melting points of all samples were in a range of 943–950 °C, which is significantly lower than the value for pure bulk Ag (961.8 °C). Every sample was measured in three heating-cooling cycles (Figs. S1–5). Unprotected Ag nanoparticles should melt in the first heating cycle displaying MPD and subsequently create the bulk material. The melting temperature of bulk Ag should be measured during the second and third cycles. MPD is determined by the difference between these values. On the other hand, the DSC measurements of the Ag@Ni core-shell nanoparticles were expected to display the depressed melting points of nano-Ag in all three runs. We indeed observed depressed melting point temperatures of nearly the same value in all three runs; moreover, the broadening of endothermic peaks in each subsequent run was evident in all five Ag@Ni samples. Presumably, the nickel shell stayed solid during heating and partly protected the silver core against sintering. At the same time, as STEM-EDS analysis [36] showed, the nickel shell did not fully encase the silver core. It results in the coagulation of a part of silver into bulk material during heating. The SEM-EDS images of residues left after completing three runs of DSC analysis (Figs. S6–13) revealed that particle size distribution gradually broadened, individual NPs partially coagulated into microparticles which caused melting to occur in a broader range. Observed broadening of endothermic peaks of silver melting during subsequent heating cycles (Figs. S1–5) is consistent with these SEM-EDS results. However, almost constant values of MPD during individual heating cycles point to the presence of a substantial portion of Ag@Ni nanoparticles. SEM-EDS showed coagulated particles composed of two separated phases, silver- and nickel-rich. A tendency to coagulation and formation of larger particles more pronounced with decreasing nickel content and less complete Ni shell, as Figs. S6–13 display. Comparison of Figs. S7 and S13 clearly illustrates this phenomenon. Fig. S7 (Ag 18.8 mol%) shows many particles with broad size distribution and separated phases, while Fig. S13 (Ag 93.9 mol%) displays only one particle composed of two separated phases.

4.2. Theoretical results

Here we describe the results of the calculation of the particle size influence on the phase transition temperatures in the AgNi alloy. The Ag–Ni system is relatively simple with minimum mutual solubility of both elements in the solid state. Also, there is a significant miscibility gap in the liquid phase, reaching very high temperatures. The bulk Ag–Ni phase diagram was calculated using the Thermo-Calc® software and the SOLDERS database, created in the scope of COST 531 project [46], and the result is shown in Fig. 2.

The contribution from the surface energy was calculated by Eq. (2), using the values of the surface stress calculated by the ab-initio approach described in Ref. [43]. The relevant values for the two elements are
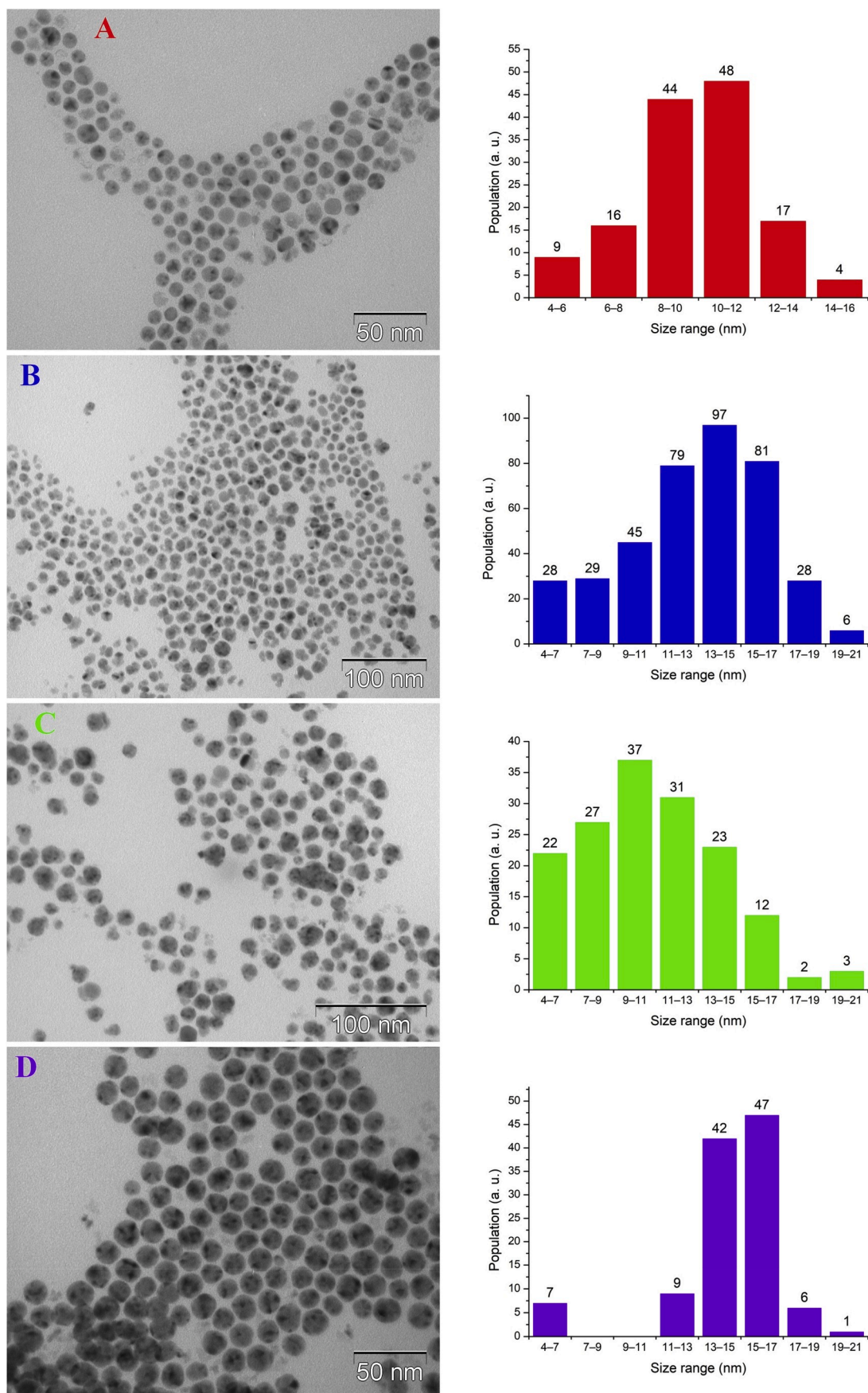
Table 1
Elemental compositions and particle diameters by the DLS, SAXS, and TEM methods. $\bar{x}$ is a weighted average of nanoparticle diameters, Z-average is the intensity-weighted mean hydrodynamic size of the ensemble collection of particles measured by DLS, D_{max} is the longest distance between two points in one nanoparticle, s is a standard deviation.

Composition (mol%)	Ag	18.79	41.07	49.29	64.4	93.92
	Ni	81.21	58.93	50.71	35.6	6.08
DLS (nm)	$\bar{x}$	32	28	30	26	23
	Z-average	32	25	25	24	22
SAXS (nm)	D_{max}	25.5	21.8	–	18.1	17.6
	s	0.49	0.44	–	0.44	0.59
TEM (nm)	$\bar{x}$	10.9	13.9	–	11.8	15.5
	s	2.28	3.56	–	3.63	2.81

Fig. 1. TEM images with corresponding size distribution histograms of as-prepared nanoparticles with various composition A: 18.79 mol%Ag $\bar{x} = 10.9$ nm, B: 41.07 mol%Ag $\bar{x} = 13.9$ nm, C: 64.4. mol%Ag $\bar{x} = 11.8$ nm, D: 93.92 mol%Ag $\bar{x} = 15.5$ nm.

Table 2
Elemental compositions, particle sizes, and DSC temperatures (±0.5 °C).

Composition (mol%)	Ag	18.79	41.07	49.29	64.4	93.92
	Ni	81.21	58.93	50.71	35.6	6.08
TEM	$\bar{x}$ **(nm)**	10.9	13.9	–	11.8	15.5
	s	2.28	3.56	–	3.63	2.81
DSC (°C)	**1st run**	944.3	947.8	946.9	948.9	947.9
	2nd run	943.5	948.0	946.8	948.9	949.8
	3rd run	943.1	949.6	946.8	949.4	949.7

Table 3
Lattice parameters a, surface energy γ, surface stress τ, and experimental molar volume V_m, for silver and nickel. The calculations of γ and τ were made for close-packed atomic plane (111).

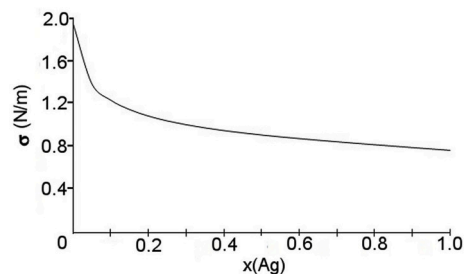| Phase (fcc cF4)	a calc. (Å)	a exp. (Å)	γ/J m^{-2} (γ non-relaxed)	τ/N m^{-1} (τ non-relaxed)	V_m/m^3 mol^{-1} ·10^{-6}
Ag	4.1478	4.0853	0.770 (0.770)	0.718 (0.778)	10.265090
Ni	3.5246	3.524	1.959 (1.965)	2.228 (2.443)	6.588689

shown in Table 3. Calculated and experimental lattice parameters of Ag and Ni are also listed in this table. The calculated lattice parameters in the scope of this work were computed for 0 K. The room temperature experimental lattice parameter for Ni is taken from Taylor [47] and that for Ag from Liu and Bassett [48]. The calculated molar volume of Ag exceeds the experimental value by only 4.7%. Furthermore, the calculated molar volume of nickel almost perfectly agrees with the experimental value (see the lattice constants in Table 3). Thus, in an attempt to reproduce the experimental data as best as possible, we have used the experimental values for the molar volume in the *CALPHAD* calculations. As explained in Ref. [14], the calculated value of the surface energy was used for the surface stress value of the liquid phase. The concentration and temperature dependence of the Gibbs energy contribution for liquid was calculated using the approach described in Ref. [43], where the interaction parameters approach equivalent to the Redlich-Kister method was applied.

The concentration dependence of the surface stress in the liquid alloy was calculated by the software developed in Ref. [44] using the Butler equation. The concentration dependence of the surface tension for the temperature of 1423 °C is shown in Fig. 3.

The influence of the particle size on the phase diagram was studied theoretically for the diameters roughly corresponding to the size of synthesized Ag@Ni NPs. The selection of the particle diameters for the purpose of the modeling was based on the TEM measurements (see Table 1 and Fig. 1). The diameter values measured by DLS and SAXS methods are larger because we presume that the envelope formed by the organic ligands is included in the measurement. No clear dependence of the particle size on the alloy composition was found; therefore, the

**Fig. 3.** The concentration dependence of the surface stress in liquid AgNi alloy for 1423 °C.

calculations were carried out for the particle diameters of 10, 15, and 20 nm (Table 4).

The melting point depression for pure Ag was found to be 21.1 °C for 15 nm diameter (961.8 → 940.7 °C) and the temperature of the (Liquid → (Ag) + (Ni)) invariant reaction decreased from 961.1 °C to 940.4 °C. For the 20 nm particles, these values are 15.8 °C (961.8 → 946.0 °C) and 945.6 °C, respectively. The overall influence of the particle size on the phase diagram is presented in Fig. 4a,b, where the phase boundaries for

Table 4
The influence of the particle size on the melting point and invariant reaction temperature for Ag@Ni NPs.

Diameter (nm)	10	15	20	Bulk
Pure Ag (°C)	930.2	940.7	946.0	961.8
Invariant reaction (°C)	930.0	940.4	945.6	961.1
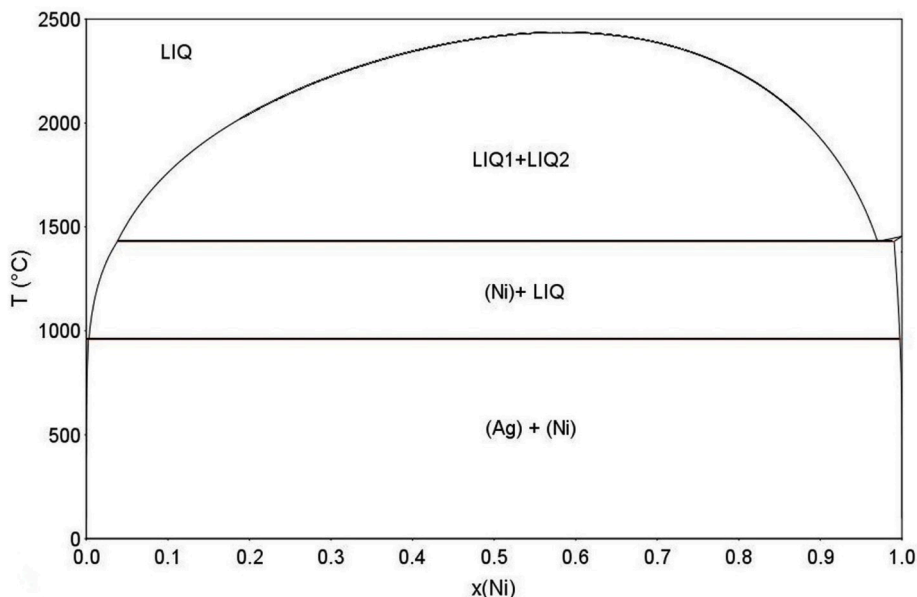
Fig. 2. The Ag–Ni phase diagram for the bulk system. Both Ag and Ni crystallize in the fcc_A1 structure.
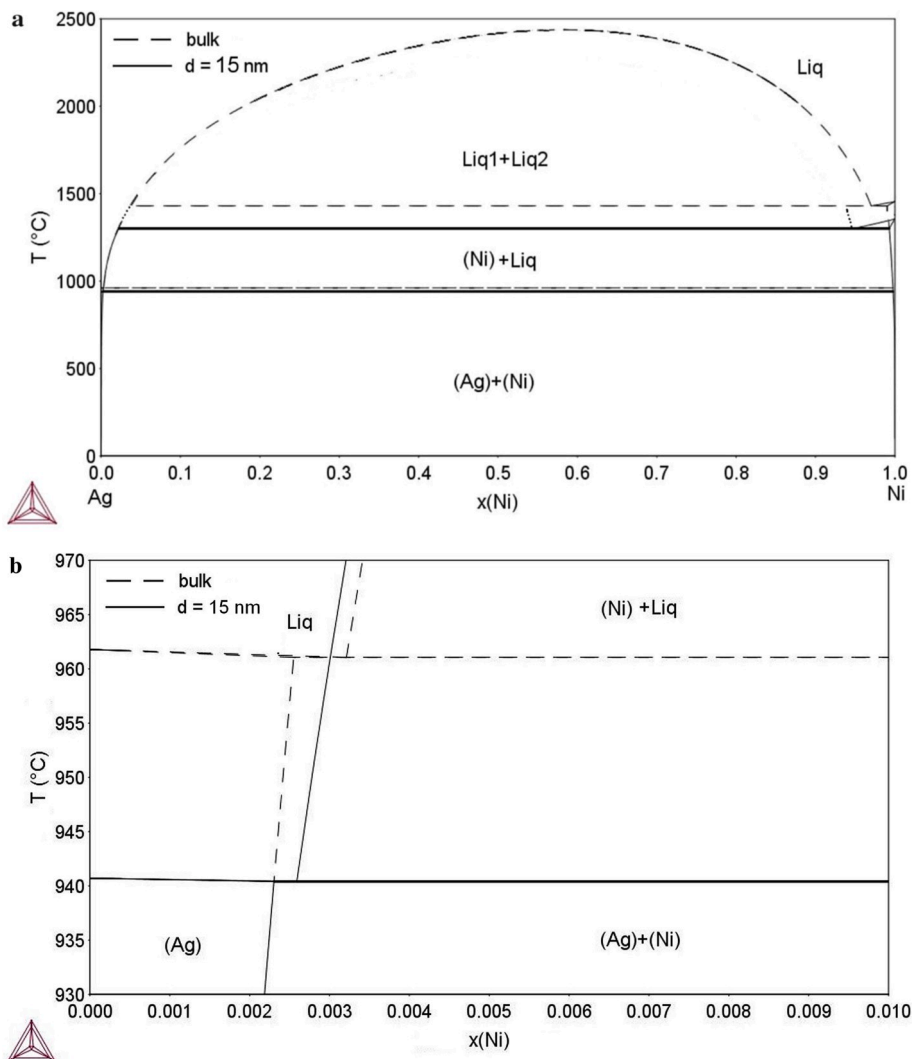
Fig. 4. a. Comparison of the equilibrium phase diagram with the phase diagram for the particle diameter of 15 nm.
b. Detail of the comparison in the Ag-rich corner.

the bulk system are shown (dashed lines) together with the phase boundaries reflecting the influence of the 15 nm nanoparticle size (solid line) on the transformation temperatures. The depression of the melting temperature as a function of composition is calculated based on Eq. (2), where the concentration dependence of surface stress was calculated by the Butler equation. In the case of the Ag–Ni system, where the liquid miscibility gap exists over a wide range of compositions, this approach cannot be used as the behavior of the liquids in the phase region within the miscibility gap cannot be described. The calculation only predicts that the miscibility gap still exists for all nanoparticle diameters at the temperature of the monotectic reaction but the behavior of the miscibility gap cannot be predicted. Therefore, the whole phase boundary of the liquid miscibility gap is not drawn in Fig. 4a.

As the nanoparticles have the core-shell structure with the Ag core, the relevant comparison of the calculated and experimentally measured transformation temperatures can be done for the melting point depression of pure silver. The experimentally measured values were obtained for Ag@Ni with different content of silver (18.8–94.0 mol%) and diameters ranging from 10.9 to 15.5 nm with standard deviations of 2.3–3.6 nm (Table 2). The actual diameter of the Ag core is apparently smaller than the nominal particle size and must also vary depending on the silver content. The experimental temperatures of 943–950 °C agree relatively well with the calculated values of 940.7 °C for 15 nm and

946.0 °C for 20 nm (Table 4) considering uncertainty in the actual Ag core diameter.

5. Conclusions

Ag@Ni core-shell nanoparticles were prepared in various Ag/Ni stoichiometric ratios, and their elemental composition was characterized by the ICP-OES method. The size distribution was analyzed by the DLS, SAXS, and TEM techniques. The dependency of the nanoparticle size on composition was not observed as all samples fall within 11–15 nm in diameter. The main focus of this work was on measuring thermal properties by the DSC method and comparison of experimental data with the Ag–Ni theoretical phase diagram, which was predicted by the *CALPHAD* method. We took advantage of immiscibility of Ag and Ni in the solid state and of the Ag@Ni core-shell structure in which the silver core encapsulated within the nickel shell was protected from sintering and coagulation during all heating cycles. The calculated melting points of pure Ag for nanoparticles of the diameter of 15 and 20 nm were 940.7 °C and 946.0 °C, respectively. These values are in good agreement with the measured melting points of 943–950 °C observed for Ag@Ni.

Appendix A. Supplementary data

Supplementary data to this article can be found online at https://doi.org/10.1016/j.calphad.2020.101741.

References

[1] G.C. Papavassiliou, Surface plasmons in small Au–Ag alloy particles, J. Phys. F Met. Phys. 6 (1976) 103–105, https://doi.org/10.1088/0305-4608/6/4/004.

[2] D. Maity, M.M.R. Mollick, D. Mondal, B. Bhowmick, S.K. Neogi, A. Banerjee, S. Chattopadhyay, S. Bandyopadhyay, D. Chattopadhyay, Synthesis of HPMC stabilized nickel nanoparticles and investigation of their magnetic and catalytic properties, Carbohydr. Polym. 98 (2013) 80–88, https://doi.org/10.1016/j.carbpol.2013.05.020.

[3] S. Mourdikoudis, K. Simeonidis, A. Vilalta-Clemente, F. Tuna, I. Tsiaoussis, M. Angelakeris, C. Dendrinou-Samara, O. Kalogirou, Controlling the crystal structure of Ni nanoparticles by the use of alkylamines, J. Magn. Magn Mater. 321 (2009) 2723–2728, https://doi.org/10.1016/j.jmmm.2009.03.076.

[4] A.C. Johnston-Peck, J. Wang, J.B. Tracy, Synthesis and structural and magnetic characterization of Ni(core)/NiO(shell) nanoparticles, ACS Nano 3 (2009) 1077–1084, https://doi.org/10.1021/nn900019x.

[5] J. Sopousek, O. Zobac, J. Bursik, P. Roupcova, V. Vykoukal, P. Broz, J. Pinkas, J. Vrestal, Heat-induced spinodal decomposition of Ag–Cu nanoparticles, Phys. Chem. Chem. Phys. 17 (2015) 28277–28285, https://doi.org/10.1039/C5CP00198F.

[6] V. Vykoukal, H. Vitezslav, B. Michal, J. Bursik, J. Pinkas, Molecular precursors for morphology control of AgCu nanoalloys, Inorg. Chem. 58 (2019) 15246–15254, https://doi.org/10.1021/acs.inorgchem.9b02172.

[7] A. Roshanghias, J. Vrestal, A. Yakymovych, K.W. Richter, H. Ipser, Sn–Ag–Cu nanosolders: melting behavior and phase diagram prediction in the Sn-rich corner of the ternary system, Calphad 49 (2015) 101–109, https://doi.org/10.1016/j.calphad.2015.04.003.

[8] J. Sopousek, J. Vrestal, J. Pinkas, P. Broz, J. Bursik, A. Styskalik, D. Skoda, O. Zobac, J. Lee, Cu–Ni nanoalloy phase diagram – prediction and experiment, Calphad 45 (2014) 33–39, https://doi.org/10.1016/j.calphad.2013.11.004.

[9] R. Ferrando, J. Jellinek, R.L. Johnston, Nanoalloys: from theory to applications of alloy clusters and nanoparticles, Chem. Rev. 108 (2008) 845–910, https://doi.org/10.1021/cr040090g.

[10] J. Havrankova, J. Vrestal, L.G. Wang, M. Sob, Ab initio analysis of energetics of σ-phase formation in Cr-based systems, Phys. Rev. B 63 (2001), 174104, https://doi.org/10.1103/PhysRevB.63.174104.

[11] J. Vrestal, J. Houserova, M. Sob, M. Friak, Calculation of phase equilibria with σ-phase in some Cr-based systems using first-principles calculation results, in: The 16th Discussion Meeting on Thermodynamics of Alloys (TOFA), May 8-11, 2000, Abstract Book, Stockholm, Sweden), 2000, p. 33.

[12] J. Lee, K.J. Sim, General equations of CALPHAD-type thermodynamic description for metallic nanoparticle systems, Calphad 44 (2014) 129–132, https://doi.org/10.1016/j.calphad.2013.07.008.

[13] G. Kaptay, Nano-Calphad: extension of the Calphad method to systems with nano-phases and complexions, J. Mater. Sci. 47 (2012) 8320–8335, https://doi.org/10.1007/s10853-012-6772-9.

[14] A. Kroupa, T. Kana, J. Bursik, A. Zemanova, M. Sob, Modelling of phase diagrams of nanoalloys with complex metallic phases: application to Ni–Sn, Phys. Chem. Chem. Phys. 17 (2015) 28200–28210, https://doi.org/10.1039/C5CP00281H.

[15] J. Sopousek, J. Vrestal, A. Zemanova, J. Bursik, Phase diagram prediction and particle characterization of Sn-Ag nano alloy for low melting point lead-free solders, J. Min. Metall. B Metall. 48 (2012) 419–425, https://doi.org/10.2298/JMMB120121032S.

[16] C. Zou, Y. Gao, B. Yang, Q. Zhai, Synthesis and DSC study on Sn3.5Ag alloy nanoparticles used for lower melting temperature solder, J. Mater. Sci. Mater. Electron. 21 (2010) 868–874, https://doi.org/10.1007/s10854-009-0009-y.

[17] L.-Y. Hsiao, J.-G. Duh, Synthesis and characterization of lead-free solders with Sn-3.5Ag-xCu (x=0.2, 0.5, 1.0) alloy nanoparticles by the chemical reduction method, J. Electrochem. Soc. 152 (2005) J105, https://doi.org/10.1149/1.1954928.

[18] A. Roshanghias, J. Vrestal, A. Yakymovych, K.W. Richter, H. Ipser, Sn–Ag–Cu nanosolders: melting behavior and phase diagram prediction in the Sn-rich corner of the ternary system, Calphad 49 (2015) 101–109, https://doi.org/10.1016/j.calphad.2015.04.003.

[19] J. Sopousek, J. Vrestal, J. Pinkas, P. Broz, J. Bursik, A. Styskalik, D. Skoda, O. Zobac, J. Lee, Cu–Ni nanoalloy phase diagram – prediction and experiment, Calphad 45 (2014) 33–39, https://doi.org/10.1016/j.calphad.2013.11.004.

[20] S. Delsante, G. Borzone, R. Novakovic, D. Piazza, G. Pigozzi, J. Janczak-Rusch, M. Pilloni, G. Ennas, Synthesis and thermodynamics of Ag–Cu nanoparticles, Phys. Chem. Chem. Phys. 17 (2015) 28387–28393, https://doi.org/10.1039/C5CP02058A.

[21] J. Sopousek, J. Pinkas, P. Broz, J. Bursik, V. Vykoukal, D. Skoda, A. Styskalik, O. Zobac, J. Vrestall, A. Hrdlicka, J. Simbera, Ag-Cu colloid synthesis: bimetallic nanoparticle characterisation and thermal treatment, J. Nanomater. 2014 (2014), https://doi.org/10.1155/2014/638964.

[22] C.L. Chen, J.-G. Lee, K. Arakawa, H. Mori, Comparative study on size dependence of melting temperatures of pure metal and alloy nanoparticles, Appl. Phys. Lett. 99 (2011), https://doi.org/10.1063/1.3607957, 013108–013111.

[23] W.A. Jesser, G.J. Shiflet, G.L. Allen, J.L. Crawford, Equilibrium phase diagrams of isolated nano-phases, Mater. Res. Innovat. 2 (1999) 211–216, https://doi.org/10.1007/s100190050087.

[24] W.A. Jesser, R.Z. Shneck, W.W. Gile, Solid-liquid equilibria in nanoparticles of Pb-Bi alloys, Phys. Rev. B 69 (2004) 144121, https://doi.org/10.1103/PhysRevB.69.144121.

[25] D. Wakuda, K. Kim, K. Suganuma, Room temperature sintering of Ag nanoparticles by drying solvent, Scripta Mater. 59 (2008) 649–652, https://doi.org/10.1016/j.scriptamat.2008.05.028.

[26] D. Wakuda, Keun-Soo Kim, K. Suganuma, Room-temperature sintering process of Ag nanoparticle paste, IEEE Trans. Compon. Packag. Technol. 32 (2009) 627–632, https://doi.org/10.1109/TCAPT.2009.2015874.

[27] K.-S. Moon, H. Dong, R. Maric, S. Pothukuchi, A. Hunt, Y. Li, C.P. Wong, Thermal behavior of silver nanoparticles for low-temperature interconnect applications, J. Electron. Mater. 34 (2005) 168–175, https://doi.org/10.1007/s11664-005-0229-8.

[28] M. Maruyama, R. Matsubayashi, H. Iwakuro, S. Isoda, T. Komatsu, Silver nanosintering: a lead-free alternative to soldering, Appl. Phys. A 93 (2008) 467–470, https://doi.org/10.1007/s00339-008-4807-5.

[29] T. Castro, R. Reifenberger, E. Choi, R.P. Andres, Size-dependent melting temperature of individual nanometer-sized metallic clusters, Phys. Rev. B 42 (1990) 8548–8556, https://doi.org/10.1103/PhysRevB.42.8548.

[30] C.L. Chen, J.-G. Lee, K. Arakawa, H. Mori, In situ observations of crystalline-to-liquid and crystalline-to-gas transitions of substrate-supported Ag nanoparticles, Appl. Phys. Lett. 96 (2010), 253104, https://doi.org/10.1063/1.3456382.

[31] C. Tang, Y.-M. Sung, J. Lee, Nonlinear size-dependent melting of the silica-encapsulated silver nanoparticles, Appl. Phys. Lett. 100 (2012), 201903, https://doi.org/10.1063/1.4712599.

[32] H. Guo, Y. Chen, X. Chen, L. Wang, H. Ping, D.-L. Peng, Preparation of bimetallic core-shell nanoparticles with magnetically recyclable and high catalytic abilities, Procedia Eng 36 (2012) 504–509, https://doi.org/10.1016/j.proeng.2012.03.073.

[33] M.D. Niry, J. Mostafavi-Amjad, H.R. Khalesifard, A. Ahangary, Y. Azizian-Kalandaragh, Formation of silver nanoparticles inside a soda-lime glass matrix in the presence of a high intensity Ar + laser beam, J. Appl. Phys. 111 (2012), 033111, https://doi.org/10.1063/1.3684552.

[34] R.J.V. Michael, B. Sambandam, T. Muthukumar, M.J. Umapathy, P.T. Manoharan, Spectroscopic dimensions of silver nanoparticles and clusters in ZnO matrix and their role in bioinspired antifouling and photocatalysis, Phys. Chem. Chem. Phys. 16 (2014) 8541, https://doi.org/10.1039/c4cp00169a.

[35] O. Niitsoo, A. Couzis, Facile synthesis of silver core – silica shell composite nanoparticles, J. Colloid Interface Sci. 354 (2011) 887–890, https://doi.org/10.1016/j.jcis.2010.11.013.

[36] V. Vykoukal, J. Bursik, P. Roupcova, D.A. Cullen, J. Pinkas, Solvothermal hot injection synthesis of core-shell AgNi nanoparticles, J. Alloys Compd. 770 (2019) 377–385, https://doi.org/10.1016/j.jallcom.2018.08.082.

[37] F. Calvo, E. Cottancin, M. Broyer, Segregation, core alloying, and shape transitions in bimetallic nanoclusters: Monte Carlo simulations, Phys. Rev. B 77 (2008), 121406, https://doi.org/10.1103/PhysRevB.77.121406.

[38] F. Baletto, C. Mottet, A. Rapallo, G. Rossi, R. Ferrando, Growth and energetic stability of AgNi core–shell clusters, Surf. Sci. 566–568 (2004) 192–196, https://doi.org/10.1016/j.susc.2004.05.044.

[39] P.V. Konarev, V.V. Volkov, A.V. Sokolova, M.H.J. Koch, D.I. Svergun, PRIMUS: a Windows PC-based system for small-angle scattering data analysis, J. Appl. Crystallogr. 36 (2003) 1277–1282, https://doi.org/10.1107/S0021889803012779.

[40] D.I. Svergun, IUCr, Determination of the regularization parameter in indirect-transform methods using perceptual criteria, J. Appl. Crystallogr. 25 (1992) 495–503, https://doi.org/10.1107/S0021889892001663.

[41] H.-L. Lukas, S.G. Fries, B. Sundman, Computational Thermodynamics – the Calphad Method, Cambridge University Press, 2007.

[42] T. Tanaka, S. Hara, Thermodynamic evaluation of nano-particle binary alloy phase diagrams, Zeitschrift Fur Met 92 (2001) 1236–1241, https://doi.org/10.11311/jscta1974.32.95.

[43] J. Park, J. Lee, Phase diagram reassessment of Ag–Au system including size effect, Calphad 32 (2008) 135–141, https://doi.org/10.1016/j.calphad.2007.07.004.

[44] R. Picha, J. Vrestal, A. Kroupa, Prediction of alloy surface tension using a thermodynamic database, Calphad 28 (2004) 141–146, https://doi.org/10.1016/j. calphad.2004.06.002.

[45] B.P. Burton, N. Dupin, S. Fries, G. Grimvall, A.F. Guillermet, P. Miodownik, W. A. Oates, V. Vinograd, Using ab initio calculations in the CALPHAD environment | NIST, Zeitschrift Fur Met 92 (2001) 514–525.

[46] A.T. Dinsdale, A. Watson, A. Kroupa, J. Vrestal, A. Zemanova, J. Vizdal, COST Action 531- Atlas of Phase Diagrams for Lead-free Soldering, 2008.

[47] A. Taylor, J. Inst. Met. 77 (1950) 585.

[48] L.G. Liu, W.A. Bassett, J. Appl. Phys. 44 (1973) 1475–1479, https://doi.org/ 10.1063/1.1662396.